catalysts

MDPI

Article

Nitrogen-Rich Porous Carbon Nanotubes Coated Co/Mo_2N Composites Derived from Metal-Organic Framework as Efficient Bifunctional Oxygen Electrocatalysts

Shiang Li [1,†], Yuehong Xie [2,†], Chao Feng [3,*], Afaq Hassan [1] and Jide Wang [1,*]

[1] Key Laboratory of Oil and Gas Fine Chemicals, Ministry of Education, Xinjiang Uygur Autonomous Region, College of Chemistry and Chemical Engineering, Xinjiang University, Urumqi 830046, China; lsa719446919@163.com (S.L.); afaq.hassan@uog.edu.pk (A.H.)
[2] Engineering Research Center of Energy Storage Materials and Devices, Ministry of Education, School of Chemistry, Xi'an Jiaotong University, Xi'an 710115, China; xieyhol@sina.com
[3] Ansteel Research Institute of Vanadium&Titanium (Iron&Steel), Chengdu 610031, China
* Correspondence: afengc@126.com (C.F.); awangjd@126.com (J.W.)
† These authors contributed equally to this work.

Abstract: Noble metal catalysts such as Pt/C and RuO_2 are the most efficient oxygen reduction reaction (ORR) and oxygen evolution reaction (OER) catalysts and show excellent activity. However, their high costs, scarcity, single function, and weak durability impede their large-scale practical application. Therefore, it is paramount to design bifunctional electrocatalysts with high activity, long durability, and low cost. In this work, we used the functionalized modification and hierarchical porous structure of MOFs and adjusted the ratio of Co/Mo atoms to prepare uniformly dispersed nanospheres. The uniform porous nitrogen-doped carbon nanotubes coated with Co/Mo_2N composites were obtained by trapping the volatile CN_x during high-temperature pyrolysis via a vapor deposition strategy. The physical and chemical properties of the materials were analyzed by various characterization methods such as XRD, XPS, TEM, SEM, Raman, and BET. Notably, CoMoN@NCNTs-700 exhibited excellent ORR/OER bifunctional electrocatalytic activity in alkaline conditions due to the synergistic effect of porous nitrogen-doped carbon nanotubes and the unique heterostructure of Co/Mo_2N. In 0.1 M KOH, its ORR half-wave potential was $E_{1/2}$ = 0.78 V, with a limiting current density even reached to 5.3 mA cm^{-2} and its operating potential was 1.60 V at a current density of 10 mA cm^{-2}. At the same time, CoMoN@NCNTs-700 also showed better stability and methanol resistance than the commercial catalysts. This work provides a valuable reference for the design and construction of inexpensive non-noble metal bifunctional electrocatalysts.

Keywords: metal-organic framework; N-doped carbon nanotubes; Co/Mo_2N unique heterostructure; bifunctional electrocatalyst

Citation: Li, S.; Xie, Y.; Feng, C.; Hassan, A.; Wang, J. Nitrogen-Rich Porous Carbon Nanotubes Coated Co/Mo_2N Composites Derived from Metal-Organic Framework as Efficient Bifunctional Oxygen Electrocatalysts. *Catalysts* **2023**, *13*, 801. https://doi.org/10.3390/catal13050801

Academic Editors: Sheng Guo, Yazi Liu and Jun Li

Received: 29 March 2023
Revised: 21 April 2023
Accepted: 23 April 2023
Published: 25 April 2023

1. Introduction

Renewable fuel cells and rechargeable zinc-air batteries are considered the most promising energy conversion and storage devices [1,2]. However, the high activation energy barrier and slow reaction kinetics of the oxygen reduction reaction (ORR) and oxygen evolution reaction (OER) restrict their practical application [3–5]. Therefore, designing efficient electrocatalysts is necessary to promote the reaction kinetics of ORRs and OERs [6]. Commercial noble metal catalytic materials Pt/C and RuO_2 are efficient ORR and OER electrocatalysts, but their shortcomings such as high cost, scarcity, and poor durability hinder further widespread application [7–9]. In addition, a single noble metal electrocatalyst cannot simultaneously perform ORR and OER electrocatalytic reactions in the same alkaline medium. Therefore, it is necessary to develop a multi-powered electrocatalyst with high efficiency, low cost, and excellent stability in a single electrolyte [10–12].

Transition metal nitrogen-doped carbon catalytic materials have the characteristics of low cost, abundant reserves, and high stability, and are thus considered potential substitutes for noble metal catalytic materials [13,14]. Metal Co has been widely used to synthesize electrocatalytic materials with good ORR activity [15,16] and Mo-based materials are abundant in reserves and have unique physical and chemical properties, such as catalytic activity similar to Pt and d-band electron characteristics, which have broad application prospects in the field of electrocatalytic material development and research. Thus, Mo_xN can be designed and studied as a catalytic material with excellent OER activity. However, single-metal component electrocatalysts are not able to achieve multi-functional catalytic performance [17]. Combined with the characteristics of single-metal components and the intermetallic interaction, the introduction of molybdenum nitride components can generate more active sites and contribute to the improvement of ORR/OER catalytic performance. The inherent properties of the carbon framework play an important role in enhancing the catalytic activity of materials and the functional modification of catalytic materials [18] while the carbon matrix is often used as the carrier for the design and synthesis of electrocatalytic materials loaded with non-noble metal nanoparticles [19]. Among them, non-noble metal nitrogen-doped carbon materials have been introduced as electrocatalysts with better activity [20,21]. Notably, nitrogen-doped carbon nanotubes, which have the advantages of thermal stability and a high specific surface area, can expose more active sites and prevent the corrosion of the electrolyte, which leads to the loss of active components, thereby further enhancing the catalytic activity of the material [22].

Metal-organic frameworks (MOFs) have the advantages of high porosity, an orderly structure, unique physicochemical properties, and easier functionalization modification, which are regarded as the ideal precursors for the pyrolysis construction of non-noble metal nitrogen-doped carbon nanomaterials [23,24]. During the pyrolysis process, the MOF precursor gradually forms a layered porous structure, and the enlarged pores further increase the porosity, which allows a greater mass transfer [25]. At the same time, the nitrogen atoms and metal centers are evenly distributed, which is beneficial to the formed carbon material for generating more active sites and showing better catalytic activity.

Before this work, Duan et al. [26] proposed a scalable surface engineering strategy using MOF to prepare a high density Co-N_x catalyst with excellent catalytic activity, with a half-wave potential of 0.82 V in 0.1 M KOH. Similarly, Li et al. [27] used solvent effects to prepare Co-N-C derived from MOFs. DFT results showed that the synergic effect of pyridine nitrogen and CoN_x accelerated ORR progression. Meanwhile, the Tafel slope of the catalyst was not compared with that of commercial Pt/C in report. Liang et al. [28] immobilized Pt NPs uniformly in a porous nitrogen-doped carbon matrix derived from ZnCo-ZIF, which is rich in cobalt monatoms (Co SAs-ZIF-NC) as multiple active sites. The half-wave potential (0.917 V) is better than that of commercial catalyst. Jia et al. [29] introduced Mo and Ir ions into the CTAB-encapsulated ZIF-67 by substitution reaction, and then used it to catalyzed oxygen evolution reaction, which showing better activity than commercial catalysts. However, as precious metal catalysts, Pt and Ir are difficult to avoid the problem of high cost. A simple strategy for preparing oxygen evolution catalysts by co-doping MoS_2 nanocrystals with Fe and Co atoms is reported by Sathiyan. [30] The electron regulation caused by doping reduces the energy barrier of OER reaction, but the mechanism of the interaction of the three metals is difficult to understand.

In this paper, MOF-derived nitrogen-doped carbon nanotubes coated with a multi-active component CoMoN@NCNT composite were synthesized by introducing volatile CN_x species through a simple assisted pyrolysis strategy. Due to the synergistic effect of abundant active sites and nitrogen-doped carbon nanotubes, the CoMoN@NCNT composites exhibited excellent ORR/OER bifunctional catalytic performance and long-term stability in the same concentration of 0.1 M KOH electrolyte. Therefore, this work provides more ideas for realizing efficient and stable multi-functional electrocatalytic reactions under the same electrolyte and improving the energy conversion efficiency of devices.

2. Results and Discussions

2.1. Characterization

As shown in Figure 1, using a simple and easy synthesis method, phosphomolybdic acid hydrate and cobalt nitrate were uniformly dissolved in a methanol solution and then reacted with organic ligand 2-MI successively to form a ZIF-67-Mo precursor. Then, the ZIF-67-Mo nanospheres were uniformly dispersed with dicyandiamide and thermally annealed in an argon atmosphere using a vapor deposition strategy to capture the volatile CN_x substance produced by the pyrolysis of dicyandiamide. The solid carbon formed at high temperature was nitrified, finally forming an electrocatalytic material with a rich defect porous carbon nanotube structure.

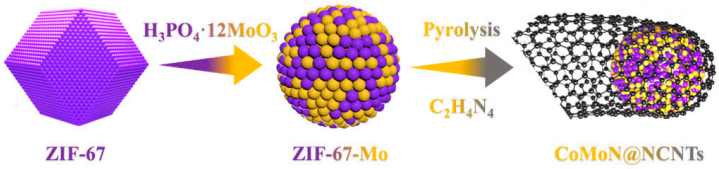

Figure 1. Schematic illustration of the fabrication process of CoMoN@NCNTs nanomaterials.

X-ray powder diffraction (XRD) spectroscopy is used to analyze the crystal structure and chemical composition of electrocatalytic materials. Figure 2a shows the crystal properties of CoMoN@NCNTs-600, CoMoN@NCNTs-700, and CoMoN@NCNTs-800 nanocomposites calcined at different temperatures. CoMoN@NCNTs series nanomaterials have three characteristic peaks at 44.2°, 51.5°, and 74.9°, corresponding to the typical (111), (200), and (220) plane of metallic cobalt, respectively [31]. The characteristic diffraction peaks of Mo_2N with 2θ values of 36.60°, 42.71°, 61.84°, and 74.22° were observed in the XRD patterns, corresponding to the (111), (200), (220), and (311) crystal planes of Mo_2N (PDF#25-1366), respectively [32]. The results showed that the nitrogen-doped carbon materials with multiple active components were formed by high-temperature calcination and the nitration of volatile CN_x species. A characteristic diffraction peak was also observed in the XRD patterns of CoMoN@NCNTs at a 2θ value of 26.43°, corresponding to the (002) crystal plane of graphite carbon [33]. In addition, compared with CoMoN@NCNTs-600, the characteristic peaks of CoMoN@NCNTs-700 and CoMoN@NCNTs-800 were sharper, indicating better crystallinity.

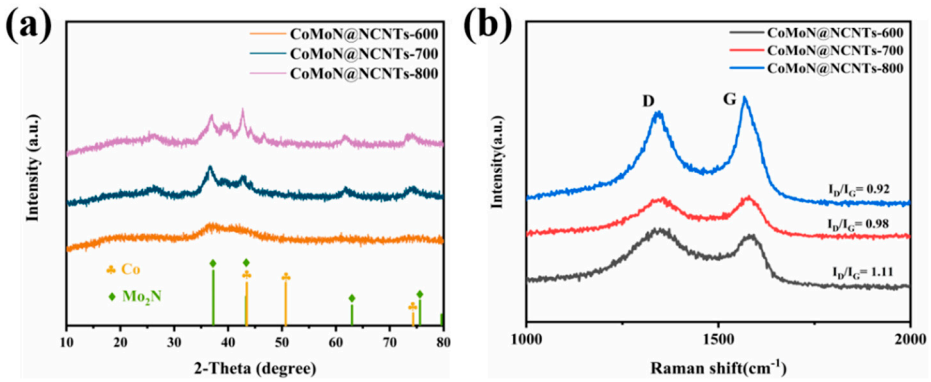

Figure 2. (**a**) XRD spectra and (**b**) Raman spectra of CoMoN@NCNTs-600, CoMoN@NCNTs-700, and CoMoN@NCNTs-800 nanocomposites.

Raman spectroscopy is used to study the state, defect, and graphitization degree of the carbon phase in carbon materials. The Raman spectra of the CoMoN@NCNTs series composites (Figure 2b) showed that there are obvious Raman characteristic peaks near 1344.9 cm^{-1} and 1579.6 cm^{-1}, which are matched with the D peak and G peak, respectively. The D band is caused by the disorder and defect of the carbon structure, and

the G band is the graphite carbon [34,35]. The strength of I_D/I_G is used to judge the degree of disorder and graphitization of carbon matrix materials. As shown in Figure 2b, the I_D/I_G values of CoMoN@NCNTs-600, CoMoN@NCNTs-700, and CoMoN@NCNTs-800 nanocomposites are 1.11, 0.98, and 0.92, respectively. With the increase in calcination temperature, the corresponding I_D/I_G strength decreases gradually, so the I_D/I_G strength of CoMoN@NCNTs-700 is moderate compared with that of CoMoN@NCNTs-600 and CoMoN@NCNTs-800, indicating that N atoms doped into the material structure and the good graphitization degree and electrical conductivity, which is conducive to the generation and uniform distribution of active sites, accelerating electron transmission in the reaction process.

The morphology and microstructure of CoMoN@NCNTs nanocomposites were investigated by SEM. Figure 3 shows the morphology changes of the CoMoN@NCNTs nanocomposites formed by ZIF-67-Mo precursors with different Co/Mo ratios at different pyrolysis temperatures. Compared with ZIF-67-Mo-1 and ZIF-67-Mo-2, Figure 3e shows the ZIF-67-Mo precursor exhibiting a clear and uniform nanosphere structure. As shown in Figure 3f, after thermal annealing, the morphology and structure of CoMoN@NCNTs-600 did not change drastically and collapsed, showing a nanosphere structure with a smaller size and slightly rough surface. However, the Raman results show that at lower carbonization temperatures, less carbon matrix is converted into graphite carbon, resulting in a lower degree of graphite and lower electrical conductivity. Figure 3g shows that the CoMoN@NCNTs-700 nanocomposites exhibited a uniform tubular structure with a large number of cracks on the surface, indicating that the shape of the ZIF-67-Mo precursor collapsed and shrunk under the continuous carbonization at 700 °C. The graphite carbon layer was thinned and heated to curl and shrink to form the nanotube structure with the synergistic effect of volatile CN_x, the active component with catalytic growth of nanotubes. CoMoN@NCNTs-700 has an abundant porous structure, which is beneficial for more active sites and provides electron/ion transport channels. The result shows that the calcination temperature is not only related to the degree of graphitization and electrical conductivity of the catalytic material but also has a great influence on the change of the porous structure and the degree of defects of electrocatalytic material.

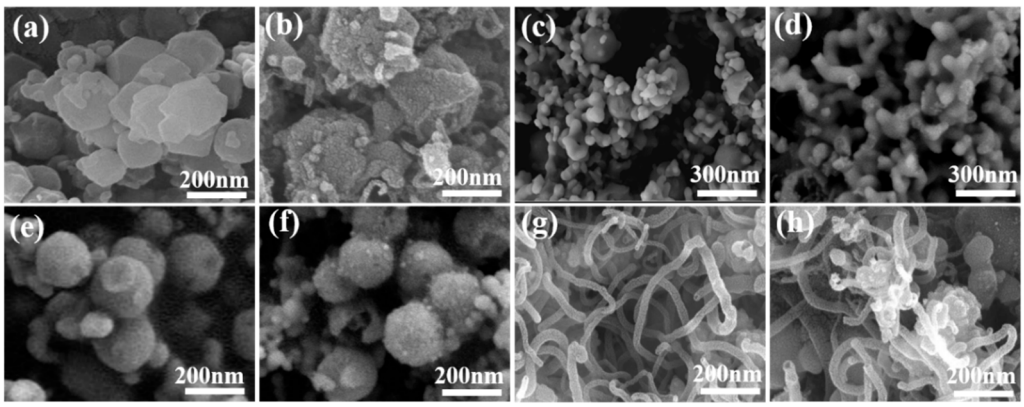

Figure 3. The SEM images: (**a**) ZIF-67-Mo-1; (**b**) CoMoN@NCNTs-700-1; (**c**) ZIF-67-Mo-2; (**d**) CoMoN@NCNTs-700-2; (**e**) ZIF-67-Mo; (**f**) CoMoN@NCNTs-600; (**g**) CoMoN@NCNTs-700; and (**h**) CoMoN@NCNTs-800.

The morphology and microstructure of the CoMoN@NCNTs nanocomposites were investigated by SEM. Figure 3 shows the morphology changes of the CoMoN@NCNT nanocomposites formed by ZIF-67-Mo precursors with different Co/Mo ratios at different pyrolysis temperatures. Compared with ZIF-67-Mo-1 and ZIF-67-Mo-2, Figure 3e shows that the ZIF-67-Mo precursor exhibits a clear and uniform nanosphere structure. As shown in Figure 3f, after thermal annealing, the morphology and structure of CoMoN@NCNTs-600 did not change drastically and collapsed, becoming a nanosphere structure with a

smaller size and slightly rough surface. However, the Raman results show that at lower carbonization temperatures, less carbon matrix is converted into graphite carbon, resulting in a lower degree of graphite and lower electrical conductivity. Figure 3g shows that the CoMoN@NCNTs-700 nanocomposites exhibited a uniform tubular structure with a large number of cracks on the surface, indicating that the shape of the ZIF-67-Mo precursor collapsed and shrunk under the continuous carbonization at 700 °C. The graphite carbon layer was thinned and heated to curl and shrink to form a nanotube structure with the synergistic effect of volatile CN_x, an active component of the catalytic growth of nanotubes. CoMoN@NCNTs-700 has an abundant porous structure, which is beneficial for providing more active sites and electron/ion transport channels. The result shows that the calcination temperature is not only related to the degree of graphitization and electrical conductivity of the catalytic material but also has a great influence on the change of the porous structure and the degree of defects of electrocatalytic material.

The internal microstructure of CoMoN@NCNTs-700 nanocomposites was further observed by TEM. Figure 4a shows the structure of hollow nanotubes which were consistent with SEM analysis. The lattice stripes of each component of the material can be clearly observed in the high-resolution transmission electron microscope image (Figure 4b). The lattice fringes of the carbon layer are 0.317 nm, corresponding to the graphite carbon (002) crystal plane, while the lattice stripe with the interlayer spacing of 0.208 nm is consistent with the Co (111) crystal plane. The lattice fringes with a spacing of 0.197 nm match the (004) crystal plane of Mo_2N. The TEM results showed that the uniform coating of multiple active components in carbon nanotubes not only effectively prevented the corrosion of metal active sites by alkaline electrolyte during an electrocatalytic reaction, but also facilitated electron transfer and the diffusion of reactant molecules, which can promote ORRs and OERs.

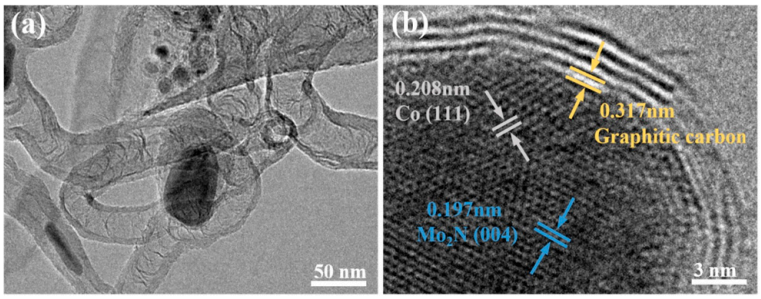

Figure 4. (**a**) TEM images; (**b**) HR-TEM images of CoMoN@NCNTs-700.

Figure 5 shows the XPS total and elemental spectra of CoMoN@NCNTs-700 nanocomposites. The characteristic peaks of Co, Mo, C, N, and O can be observed in the total spectrum of Figure 5a, indicating that the CoMoN@NCNTs-700 nanocomposite is composed of Co, Mo, C, N, and O elements. The detected oxygen element is due to the adsorption of water molecules and oxygen molecules from the air on the surface of the material during the storage process. The high-resolution Co 2p spectrum (Figure 5b) shows two sets of main peaks: the binding energies at 778.67 eV and 781.27 eV are a set of Co $2p^{3/2}$ characteristic peaks, and the binding energies at 793.76 eV and 796.81 eV are Co $2p^{1/2}$ characteristic peaks; two characteristic peaks at 784.45 eV and 801.55 eV match the satellite peaks [36]. The high-resolution Mo 3d spectrum (Figure 5c) can be fitted with three characteristic peaks with binding energies of 228.43 eV, 231.72 eV, and 235.58 eV, which belong to Mo^{2+}, Mo^{4+}, and Mo^{6+}, respectively, corresponding to the main species of Mo_2N [32]. The detected Mo^{4+} and Mo^{6+} characteristic peak signals also indicate that there may be a slight oxidation phenomenon on the surface of the sample.

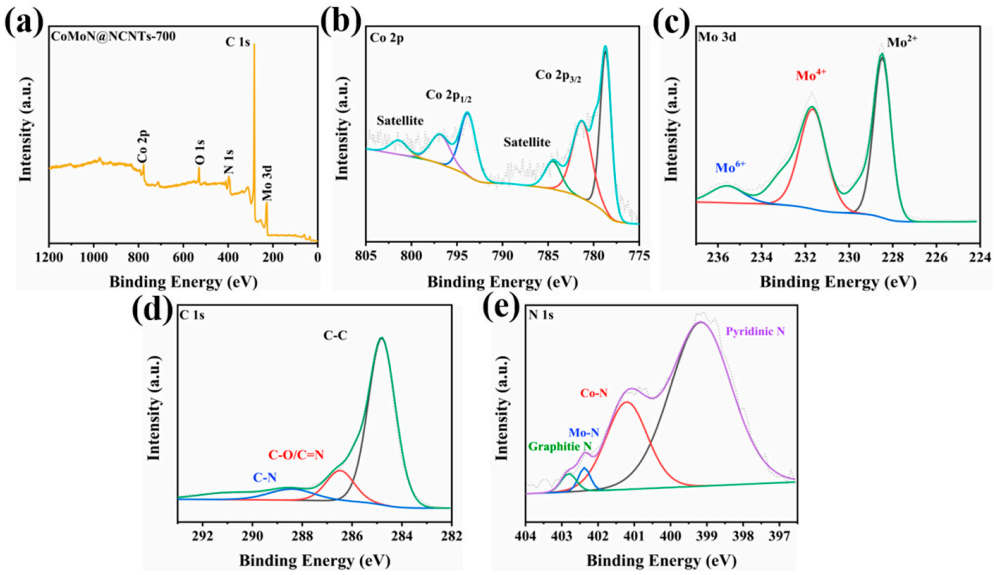

Figure 5. (**a**) XPS wide-scan spectrum; high-resolution XPS spectra of (**b**) Co 2p; (**c**) Mo 3d; (**d**) N 1s; and (**e**) C 1s levels for CoMoN@NCNTs-700.

As shown in the C 1s spectrum (Figure 5e), characteristic peaks at 284.84 eV, 286.48 eV, and 288.52 eV can be observed, corresponding to C-C, C-N, and C=O bonding states, respectively. The C-N bonding state with binding energy at 286.48 eV indicates that nitrogen atoms are doped into the carbon structure of the material. The fitting N 1s spectra (Figure 5d) shows four characteristic peaks with binding energies at 399.17 eV, 401.28 eV, 402.38 eV, and 402.88 eV, which matched with pyridine nitrogen, Co-N, Mo-N, and graphite nitrogen, respectively. The characteristic peaks of nitrogen species further confirmed the existence of structurally stable nitrogen elements in CoMoN@NCNTs-700 nanocomposites, and that metal nitrogen, pyridine nitrogen, and graphitic nitrogen active species play important roles in the ORR and OER processes. Metal and pyridine nitrogen as active sites can weaken the adsorption energy barrier of gas molecules on the carbon matrix and can also effectively promote the electron transfer process, while graphitic nitrogen helps to improve the electrical conductivity of nanomaterials. The coexistence of pyridine, metal, and graphite nitrogen contributes to the high activity of ORR and OER bifunctional CoMoN@NCNTs-700 nanocomposites.

Nitrogen adsorption and desorption curves were used to characterize the specific surface area and pore size distribution of CoMoN@NCNTs-700 nanocomposites. Figure 6 shows the nitrogen adsorption-desorption isotherm and pore size distribution of electrocatalytic materials. The specific surface area of CoMoN@NCNTs-700 is 69.19 m^2 g^{-1}, and the type IV nitrogen adsorption-desorption curve can be observed in Figure 6a, which revealed the mesoporous structure of the CoMoN@NCNTs-700 catalytic material. The corresponding pore size distribution diagram (Figure 6b) shows the layered pore size distribution above 2 nm, which further confirms the pore structure characteristics of mesopores. The CoMoN@NCNTs-700 nanocomposite has a rich porous structure that exposes more active sites, provides abundant channels for mass transfer in the reaction process, and contributes to the improvement in ORR and OER bifunctional catalytic performance.

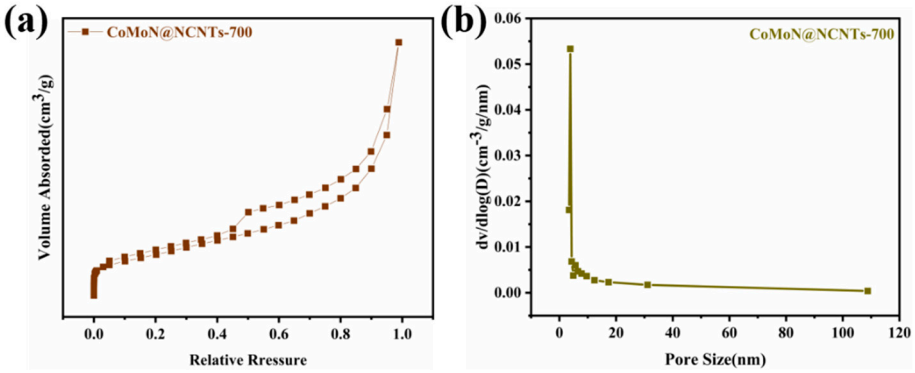

Figure 6. (**a**) N_2 adsorption-desorption isotherms; (**b**) pore diameter distribution determined by BET method of CoMoN@NCNTs-700.

2.2. Catalytic Properties

The characteristic structure of the CoMoN@NCNTs nanocomposite shows that the morphology and structure are beneficial for improving the catalytic activity of the material and promoting ORR and OER. The ORR and OER bifunctional electrocatalytic performance of samples was tested by using a three-electrode system in 0.1 M KOH electrolyte and compared with widely used commercial Pt/C and RuO_2, respectively. In the main text, we mainly compare the catalytic performance of the sample prepared by the best Co/Mo proportional precursor and performance comparisons with other samples are included in Supplementary Materials. In all measurements, the scan rate of CV was 50 mV s^{-1}, and the scan rate of LSV was 5 mV s^{-1}. Firstly, the ORR properties of porous and ultrathin carbon nanotube series electrocatalytic materials CoMoN@NCNTs with rich defects were evaluated. Figure 7a shows the CV curves of electrocatalytic samples which were prepared at different calcination temperatures. Each sample has a cathodic peak, indicating that the samples prepared at different carbonization temperatures may all show oxygen reduction properties. It is worth noting that compared with CoMoN@NCNTs-600 and CoMoN@NCNTs-800, CoMoN@NCNTs-700 had a higher current density where the peak appeared, indicating that it may have better catalytic activity. Compared with CoMoN@NCNTs-600 and CoMoN@NCNTs-800 nanocomposites, CoMoN@NCNTs-700 had the highest peak current density of ORR active reduction, indicating that CoMoN@NCNTs-700 is expected to promote the ORR process efficiently. As seen in Figure 7b, CoMoN@NCNTs-700 shows good ORR activity with a half-wave potential of $E_{1/2}$ = 0.78 V, which is better than CoMoN@NCNTs-600 ($E_{1/2}$ = 0.75 V) and CoMoN@NCNTs-800 ($E_{1/2}$ = 0.73 V). It is also better than the performance of samples prepared at 700 °C with different CoMo ratios (Figure S1). It can be seen that the LSV polarizing curve of CoMoN@NCNTs-700 is closer to the commercial Pt/C. Compared with CoMoN@NCNTs-600 and CoMoN@NCNTs-800, CoMoN@NCNTs-700 had the highest limiting current density, reaching 5.3 Ma cm^{-2}, and was even higher than commercial Pt/C. These results indicate that CoMoN@NCNTs-700 has better ORR catalytic activity compared with other samples and is consistent with the highest reduction peak value of CoMoN@NCNTs-700 in the CV curve. The Tafel curve obtained from the LSV polarization curve of the electrocatalytic sample at 1600 rpm is an important indicator of the kinetics of the ORR. Figure 7c shows that the Tafel slopes of CoMoN@NCNTs-600, CoMoN@NCNTs-700, CoMoN@NCNTs-800, and Pt/C are 63.24 Mv dec^{-1}, 54 Mv dec^{-1}, 56.45 Mv dec^{-1}, and 89.07 Mv dec^{-1}, respectively. The Tafel slopes of the CoMoN@NCNTs samples at different temperatures are all smaller than those of Pt/C; amongst all the Tafel slopes, CoMoN@NCNTs-700 is the smallest, indicating excellent ORR kinetics.

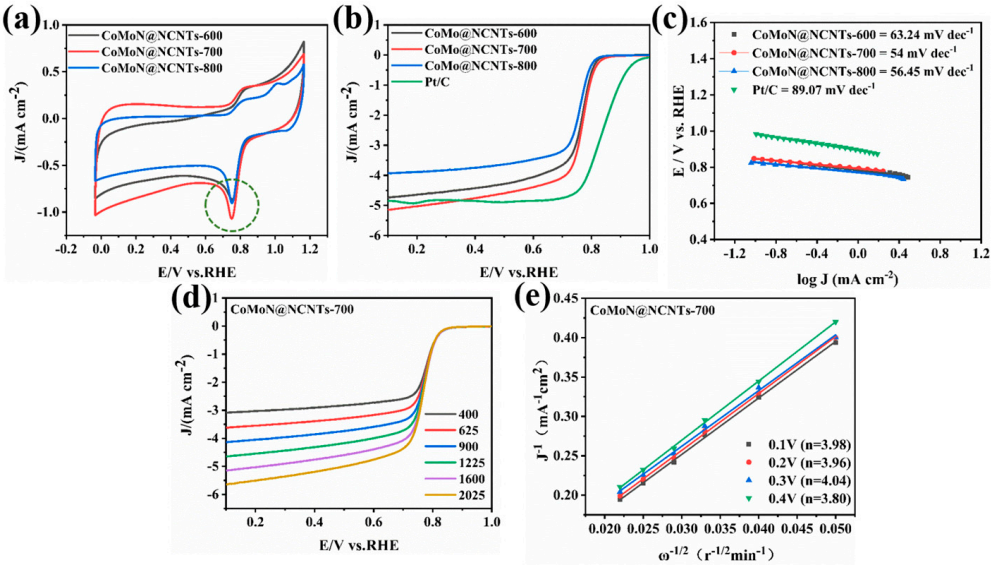

Figure 7. Electrocatalytic ORR tests of CoMoN@NCNTs and commercial Pt/C in O_2-saturated 0.1 M KOH: (**a**) CV measurement; (**b**) linear sweep voltammetry (LSV) measurements with a rotating speed of 1600 rpm; (**c**) Tafel diagram; (**d**) LSV diagram of CoMoN@NCNTs-700 at different rotation rates; and (**e**) I K–L curve under different potentials of CoMoN@NCNTs-700.

In order to explore the electron transfer process and reaction pathway of the CoMoN @NCNTs composite in the ORR, the LSV polarization curves at different rotational speeds from 400 to 2025 rpm were tested. Figure 7d shows that the limiting current density of CoMoN@NCNTs-700 increases gradually with the increase in rotational speed, which is due to decreases in diffusion length. From the LSV polarization curves of the CoMoN @NCNTs-700 nanocomposite at different rotational speeds and K–L equations, a nearly parallel K–L curve with a good linear relationship was constructed (Figure 7e). It shows that the electron transfer numbers are 3.98, 3.96, 4.04, and 3.80 from 0.1 V to 0.4 V, values that are all close to 4.0 and indicate that the ORR electrocatalytic process of CoMoN@NCNTs-700 is a four-electron reaction pathway, which is beneficial for providing a faster oxygen reduction rate and promoting the ORR.

The electron transfer number and selectivity of CoMoN@NCNTs-700 during the ORR can be further verified by the ring-rotating disk electrode test. The ring current I_R and disk current I_D were obtained from LSV polarization curves tested by RRDE at 1600 rpm, which can estimate the hydrogen peroxide yield and electron transfer number more accurately. As seen in Figure 8b, the average number of electron transfers in CoMoN@NCNTs-700 is close to 4.0 and the yield of hydrogen peroxide is between 10 and 20%, indicating that the catalytic reaction process of CoMoN@NCNTs-700 is dominated by the four-electron ($4e^-$) reduction path and that the main product is water, which is consistent with the results calculated by the K-L equation.

The long-term stability and methanol resistance of electrocatalytic materials during the catalytic reaction are also important indicators for evaluating ORR performance. The stability and durability of CoMoN@NCNTs-700 and Pt/C were measured by chronoamperometry at a potential of 0.665 V relative to the reversible hydrogen potential. Figure 8c shows that after a continuous reaction of 18,000 s, the relative current retention rate of CoMoN@NCNTs-700 was about 91.03%, which is much higher than that of Pt/C (54.13%). This is due to the protective effect of the carbon nanotube structure on the active component, which also increases the possibility of material reuse. The methanol resistance of electrocatalytic materials was also tested by the i-t test method, as shown in Figure 8d; after methanol injection, the current density of commercial Pt/C decreased sharply due to methanol poisoning, while the current density of CoMoN@NCNTs-700 did not change signif-

icantly before and after adding methanol, indicating that CoMoN@NCNTs-700 has excellent methanol resistance compared with Pt/C, which is beneficial for practical applications.

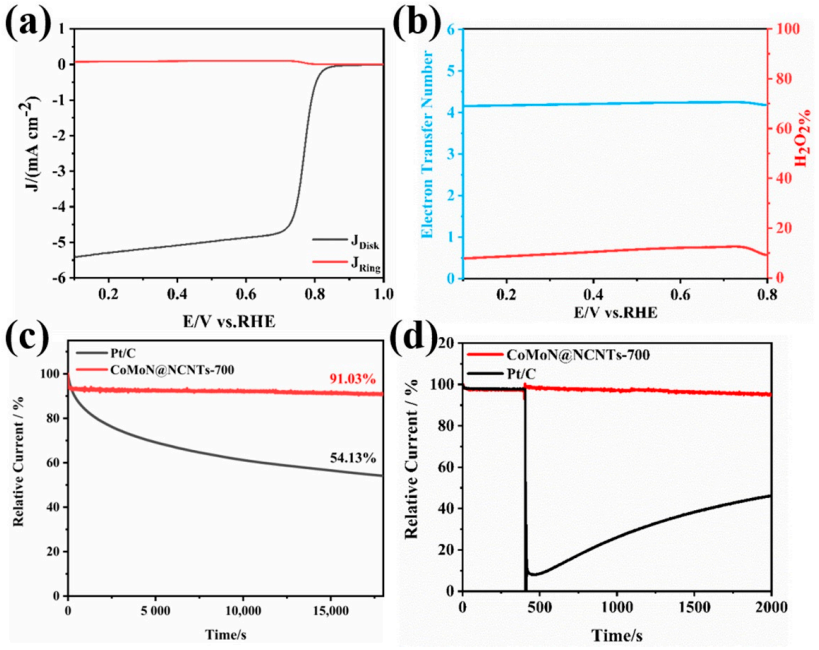

Figure 8. (**a**) RRDE LSV at rotating speeds of 1600 rpm of CoMoN@NCNTs-700; (**b**) the electron transfer number and H_2O_2 yield of CoMoN@NCNTs-700; (**c**) the i-t chronoamperometric stability measurement, and (**d**) the ethanol tolerance test of CoMoN@NCNTs-700 and Pt/C.

The OER properties of the CoMoN@NCNT series electrocatalytic materials and commercial RuO_2 were tested under the same test conditions. LSV polarization curves in the potential range of 1.0 V–2.0 V (relative to reversible hydrogen potential) were tested at 1600 rpm and a scanning rate of 5 mV s^{-1}. As shown in Figure 9a, the operating electrical potential of CoMoN@NCNTs-700 was 1.60 V at a current density of 10 mA cm^{-2} and was lower than that of CoMoN@NCNTs-600 (1.78 V) and CoMoN@NCNTs-800 (1.71 V) nanocomposites, and it also has the best oxygen evolution activity compared with the samples prepared at 700 °C with different CoMo ratios (Figure S3). Noteworthily, it was even better than that of commercial RuO_2, which operates at 1.62 V. The Tafel slope of different samples was calculated by LSV curves according to the Tafel equation to further study the OER kinetics of electrocatalytic materials. The Tafel diagram (Figure 9b) shows that the Tafel slopes of CoMoN@NCNTs-600, CoMoN@NCNTs-700, CoMoN@NCNTs-800, and commercial RuO_2 were 140.21 mV dec^{-1}, 82.83 mV dec^{-1}, 102.64 mV dec^{-1}, and 98.41 mV dec^{-1}, respectively. The Tafel slope of CoMoN@NCNTs-700 is the smallest, which indicates faster OER kinetics.

The double-layer capacitance (C_{dl}) is also a key parameter for evaluating the OER activity of electrocatalytic materials. As shown in Figure 9c, a series of CV curves were obtained by cyclic voltammetry at different scanning rates of 2, 4, 6, 8, and 10 mV s^{-1} within the potential range of 1.165 V–1.215 V in the non-Faraday region, and then the C_{dl} values of different samples were calculated. As shown in Figure 9d, the highest C_{dl} value of CoMoN@NCNTs-700 was 19.5 mF cm^{-2}, which was higher than that of CoMoN@NCNTs-600 (3.9 mF cm^{-2}) and CoMoN@NCNTs-800 (15.6 mF cm^{-2}). The higher double-layer capacitance indicates that CoMoN@NCNTs-700 has a larger electrochemical active surface area and can expose more OER active sites, which is conducive to the oxygen evolution reaction. Figure 9e shows the LSV curve comparison of CoMoN@NCNTs-700 nanocomposite before and after 1000 cycles of a cyclic voltammetry test. The results show that CoMoN@NCNTs-700 manifests long-term stability with scarce degradation at a lower operating voltage after 1000 cycles. The charge transfer resistance (R_{ct}) of CoMoN@NCNTs

electrocatalysts can be estimated from EIS. According to Figure 9f, Nyquist plots show that the resistance of CoMoN@NCNTs-600, CoMoN@NCNTs-700, and CoMoN@NCNTs-800 are 80.87 Ω, 19.52 Ω, and 26.91 Ω, respectively. Among them, the semicircular radius of the CoMoN@NCNTs-700 nanocomposite is smaller than that of other series samples, indicating that CoMoN@NCNTs-700 has small resistance and good electrical conductivity, which can accelerate charge transfer in an ORR/OER.

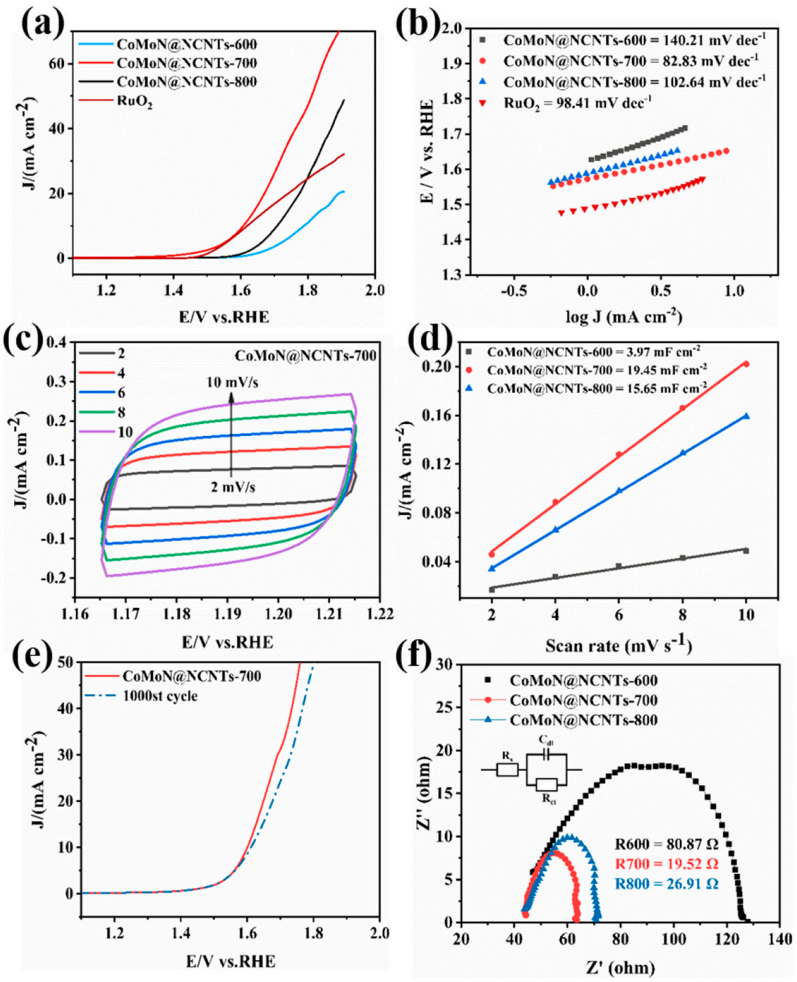

Figure 9. OER performance of the CoMoN@NCNTs nanocomposites and RuO_2 in a 0.1 M KOH solution: (**a**) LSV at a rotating speed of 1600 rpm; (**b**) OER Tafel plots; (**c**) CV measured at different scan rates from 2 to 10 mV s^{-1}; (**d**) capacitive currents at 1.195 V as a function of scan rate; (**e**) LSV curves of CoMoN@NCNTs before and after 1000 cycles; and (**f**) EIS Nyquist plots at a potential of 1.643 V.

Figure 10 shows the linear sweep voltammograms of a series of electrocatalytic samples recorded in a 0.1 M KOH alkaline solution which indicate the excellent bidirectional activity of CoMoN@NCNTs-700 electrocatalytic material for ORRs and OERs. This can be evaluated by the potential difference (ΔE) between the OER potential corresponding to the current density at 10 mA cm^{-2} and the ORR half-wave potential. Figure 10 shows that the ΔE value of CoMoN@NCNTs-700 is 0.82 V (relative to RHE), a smaller ΔE indicates a lower efficiency loss and better oxygen electrocatalytic activity. The results confirm that the CoMoN@NCNTs-700 nanocomposite has excellent ORR/OER dual-function electrocatalytic activity in a low-concentration alkaline medium and has the potential to be a candidate material for the commercial application of a zinc-air battery.

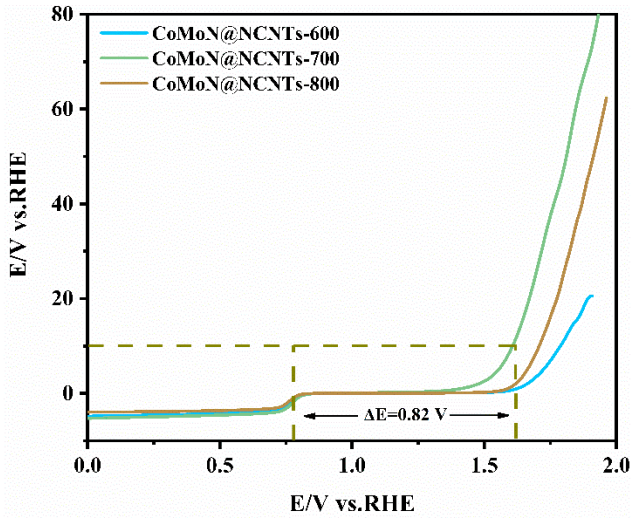

Figure 10. LSV curves of the CoMoN@NCNTs series nanocomposites showing the bifunctional ORR/OER activities in 0.1 M KOH at 1600 rpm.

3. Materials and Methods

3.1. Materials

Cobaltous nitrate ($Co(NO_3)_2$), dicyandiamide ($C_2H_4N_4$), 2-methylimidazole (2-MI), and phosphomolybdic acid ($H_7(P(Mo_2O_7)_6 \cdot \times H_2O$ were obtained from Aladdin. All reagents are analytical grade and used without further purification.

3.2. Preparation of ZIF-67-Mo Precursor

The ZIF-67-Mo precursor (Co/Mo = 1:1) materials were prepared by the co-precipitation method at room temperature. Phosphomolybdic acid hydrate was dissolved in a methanol solution, and a yellow transparent solution was formed by sonication. The cobalt nitrate hexahydrate and 2-MI were dissolved in the methanol solution, separately, and sonicated for 30 s to dissolve completely; then, a purple solution was formed by uniform mixing. After 5 min, the methanol solution of phosphomolybdic acid was added dropwise into the mixture at an appropriate rate and stirred vigorously for 30 min. After stirring, it was naturally aged for 24 h. Then, the precursor was washed with the methanol solution several times and vacuum-dried at 60 °C to obtain a powder labeled as ZIF-67-Mo (the comparison precursors with Co/Mo atomic ratios of 2:1 and 1:2 were labeled ZIF-67-Mo-1 and ZIF-67-Mo-2, respectively).

3.3. Preparation of CoMoN@NCNTs Nanocomposites

CoMoN@NCNTs were prepared by the high-temperature pyrolysis of ZIF-67-Mo with a dicyandiamide-assisted synthesis strategy. Argon gas with a sufficient steady flow was continuously pumped into the tube furnace to maintain an inert gas atmosphere. A total of 0.1 g of ZIF-67-Mo powder and 0.5 g of dicyandiamide were placed on both ends of the quartz boat, and the temperature was increased to 300 °C from room temperature at a heating rate of 2 °C min^{-1} for 1 h. The temperature was increased to the target carbonization temperature (600 °C, 700 °C, and 800 °C) at a rate of 2 °C min^{-1}. After carbonization for 2 h, black powder was obtained and labeled as CoMoN@NCNTs-600, CoMoN@NCNTs-700, and CoMoN@NCNTs-800, according to the target temperature. The samples thermally treated at 700 °C with ZIF-67-Mo-1 and ZIF-67-Mo-2 as precursors were labeled as CoMoN@NCNTs-700-1 and CoMoN@NCNTs-700-2.

3.4. The Characterization of CoMoN@NCNTs Nanocomposites

X-ray diffraction (XRD) patterns were measured on a Bruker D8 X-ray diffractometer under Cu-Ka radiation (λ = 1.5418 Å) in the 2θ range between 10° and 80°. Raman spectral

data were measured by a 488 nm laser-excited Raman spectrometer (Renishaw 1000B). Morphological and structural characterization were tested on a TESCAN MIRA LMS scanning electron microscope (accelerating voltage, 15 kV) and transmission electron microscope (TEM) and were mapped on an FEI Talos F200X microscope (accelerating voltage, 200 kV). The elemental composition and valence states of the CoMoN@NCNTs nanocomposites were analyzed by Thermo Scientific K-Alpha (XPS) spectroscopy. The system was operated at 15 kW with a monochrome Al Kα source. The specific surface area and pore size distribution of the nanotube materials were calculated by using the Brunauer–Emmett–Teller (BET) method, the model was Micromeritics APSP 2460.

3.5. Electrocatalytic Performance

All electrochemical tests were performed on an electrochemical workstation (CHI 760E) with a three-electrode system. The working electrode was prepared by a rotating disk electrode (RDE) or rotating ring disk electrode (RRDE) and silver/silver chloride reference electrode or platinum wire counter electrode, respectively. All test potential ranges and related calculations in this paper were converted to relative hydrogen standard potentials by the standard calibration equation $E_{(RHE)} = E_{(Ag/AgCl)} + 0.197\ V + 0.059 \times pH$. The 5 mg electrocatalytic sample was dissolved in 480 µL of isopropanol, 480 µL of an aqueous solution, and 40 µL of Nafion solution to form 1000 µL of dispersion liquid, which was sonicated for 30 min to form a uniformly dispersed catalyst ink. In total, 10 µL of ink was evenly dropped onto the smooth surface of the mechanically polished glassy carbon disk electrode (diameter = 5 mm, A = 0.19625 cm^2) and dried naturally at room temperature to obtain a working electrode with catalyst film.

In this paper, the electrochemical oxygen reduction reaction (ORR) catalytic performance of nanocomposites was investigated in an oxygen-saturated 0.1 M potassium hydroxide solution at a potential range of 0 V–1.0 V; the CV curve and LSV polarization curve corresponding to the electrocatalytic material were obtained by the cyclic voltammetry method and the linear sweep voltammetry method, respectively. The scan rate of the CV test was 50 mV s^{-1}, and the scanning rate of the LSV polarization curves at different rotation rates from 400 to 2025 rpm was 5 mV s^{-1}. The electron transfer number during the ORR is calculated by the Koutecky–Levich (K-L) equation [37]:

$$1/J = 1/J_L + 1/J_K = 1/B\omega^{1/2} + 1/J_K \quad (1)$$

$$B = 0.62nFC_0(D_0)^{2/3}\nu^{-1\backslash 6} \quad (2)$$

$$J_K = nFkC_0 \quad (3)$$

where J is the current density, including J_K, which is the kinetically limited current density; B is the inverse of the slope of the K-L curve obtained from different speeds; ω is the rotation rate of the catalyst-coated working electrode; F is the Faradaic efficiency of 96,485 C mol^{-1}; C_0 (1.2×10^{-6} mol cm^{-3}) and D_0 (1.9×10^{-5} cm^2 s^{-1}) are the overall concentration and diffusion coefficient of O_2 molecules, respectively; and ν is the kinematic viscosity of 0.01 cm^{-2} s^{-1}.

In addition, the LSV polarization curve obtained by the RRDE test can further evaluate the electron transfer number and hydrogen peroxide yield of the electrocatalytic material during the ORR [38]:

$$N = 4 \times I_D/(I_R/N + I_D) \quad (4)$$

$$H_2O_2\% = 200 \times (I_R/N)/(I_R/N + I_D) \quad (5)$$

where I_R is the current density of the disk electrode during the RRDE test; I_D is the current density of the disk electrode; and N (0.37) is the Pt ring collection efficiency on RRDE.

The long-term stability and methanol resistance of CoMoN@NCNTs nanocomposites and commercial Pt/C were measured by chronoamperometry.

The OER electrochemical measurements of the electrocatalytic samples were also carried out by rotating disk electrodes in an O_2-saturated 0.1 M KOH electrolyte. The LSV polarization curve of the OER was measured at 1600 rpm with a scan potential range of 1.0 V–2.0 V and a scan rate is 5 mV s^{-1}. All electrochemical tests in this paper have been corrected for internal resistance (IR) compensation.

4. Conclusions

In summary, a facile and feasible synthetic strategy was proposed. MOF-derived nitrogen-doped carbon nanotubes coated with multi-active component CoMoN@NCNT nanocomposites were prepared by the dicyandiamide-assisted pyrolysis of ZIF-67-Mo nanosphere precursors capturing volatile CN_x. The CoMoN@NCNTs-700 nanocomposite exhibited excellent ORR and OER bifunctional activity and good stability; its stability was shown to be better than that of commercial Pt/C after a continuous reaction of 18,000 s. The relative current retention rate of CoMoN@NCNTs-700 was about 91.03% and it had the lowest Tafel slope (54 mV dec^{-1}). Compared with commercial RuO_2, it had a better overpotential of up to 370 mV. Furthermore, the tubular structure of CoMoN@NCNTs-700, an evenly distributed ordered structure, can prevent the agglomeration of nanoparticles and the loss of active components. Abundant microporous structures expose more active sites, increase the contact area between reactants and catalytic active sites, and accelerate electron and ion transport to facilitate the reaction process. At the same time, with the action of metal particles, metal-nitrogen, pyridine nitrogen, and other active components, the bifunctional catalytic performance of the material is further enhanced.

Supplementary Materials: The following supporting information can be downloaded at: https://www.mdpi.com/article/10.3390/catal13050801/s1, Figure S1: the LSV of a series of prepared composites at a rotating speed of 1600 rpm for ORR in 0.1 M KOH; Figure S2: the LSV of (a) CoMoN@NCNTs-600 and (b) CoMoN@NCNTs-800 with different rotating speeds (400 to 2025 rpm) in 0.1 M KOH; K-L curves of (c) CoMoN@NCNTs-600, and (d) CoMoN@NCNTs-800; Figure S3: the LSV of series of prepared composites at a rotating speed of 1600 rpm for OER in 0.1 M KOH; Figure S4: CV of CoMoN@NCNTs-600 measured at different scan rates from 2 to 10 mV s^{-1}; Figure S5: CV of CoMoN@NCNTs-800 measured at different scan rates from 2 to 10 mV s^{-1}; Figure S6: ORR Tafel plots of CoMoN@NCNTs-700, CoMoN@NCNTs-700-1, and CoMoN@NCNTs-700-2; Figure S7: OER Tafel plots of CoMoN@NCNTs-700, CoMoN@NCNTs-700-1, and CoMoN@NCNTs-700-2; Table S1: ORR and OER activities of previously reported bifunctional electrocatalysts at 1600 rpm.

Author Contributions: Conceptualization, Investigation, Methodology, Data curation, Writing-Original draft preparation, Writing—review and editing, S.L.; Conceptualization, Writing—review and editing, Methodology, Validation, Software, Y.X.; Conceptualization, Writing—review and editing, Methodology, Validation, Software, C.F.; Writing—review and editing Validation, Software, A.H.; Funding acquisition, Project administration, Supervision, Writing—review and editing, J.W. All authors have read and agreed to the published version of the manuscript.

Funding: This research was funded by the National Natural Science Foundation of China (grant number 22169018, 21861035) and the Tianchi Hundred People Plan Project Foundation of Xinjiang Uygur Autonomous Region (grant number TCBR202103).

Data Availability Statement: Data are contained within the article.

Acknowledgments: In this section, you can acknowledge any support given which is not covered by the author contribution or funding sections. This may include administrative and technical support, or donations in kind (e.g., materials used for experiments).

Conflicts of Interest: The authors declare no conflict of interest.

References

1. Wang, H.J.; Song, Y.; Cao, Y.; Yu, H.; Peng, F. Facile Synthesis of cobalt and nitrogen coordinated carbon nanotube as a high-Performance electrocatalyst for oxygen reduction reaction in both acidic and alkaline media. ACS Sustain. *Chem. Eng.* **2019**, *7*, 10951–10961. [CrossRef]
2. Yang, J.; Chang, L.; Guo, H.; Sun, J.; Xu, J.; Xiang, F.; Zhang, Y.; Wang, Z.; Wang, L.; Hao, F.; et al. Electronic structure modulation of bifunctional oxygen catalysts for rechargeable Zn-air batteries. *J. Mater. Chem. A* **2019**, *8*, 1229–1237. [CrossRef]
3. Yan, Q.; Sun, R.-M.; Wang, L.-P.; Feng, J.-J.; Zhang, L.; Wang, A.-J. Cobalt nanoparticles/nitrogen, sulfur-codoped ultrathin carbon nanotubes derived from metal organic frameworks as high-efficiency electrocatalyst for robust rechargeable zinc-air battery. *J. Colloid Interface Sci.* **2021**, *603*, 559–571. [CrossRef] [PubMed]
4. Zhu, C.; Ma, Y.; Zang, W.; Guan, C.; Liu, X.; Pennycook, S.J.; Wang, J.; Huang, W. Conformal dispersed cobalt nanoparticles in hollow carbon nanotube arrays for flexible Zn-air and Al-air batteries. *Chem. Eng. J.* **2019**, *369*, 988–995. [CrossRef]
5. Martini, B.K.; Maia, G. Using a combination of Co, Mo, and Pt oxides along with graphene nanoribbon and $MoSe_2$ as efficient catalysts for OER and HER. *Electrochim. Acta* **2021**, *391*, 138907. [CrossRef]
6. Zhang, T.; Zhang, B.; Peng, Q.; Zhou, J.; Sun, Z. Mo_2B_2 MBene-supported single-atom catalysts as bifunctional HER/OER and OER/ORR electrocatalysts. *J. Mater. Chem. A* **2021**, *9*, 433–441. [CrossRef]
7. Yin, J.; Jin, J.; Liu, H.; Huang, B.; Lu, M.; Li, J.; Liu, H.; Zhang, H.; Peng, Y.; Xi, P.; et al. $NiCo_2O_4$-based nanosheets with uniform 4 nm mesopores for excellent Zn-air battery performance. *Adv. Mater.* **2020**, *32*, e2001651. [CrossRef]
8. Wang, W.; Wang, H.; Yu, Y.; Wu, Z.; Asif, M.; Liu, H. Metallic cobalt modified MnO-C nanocrystalline composites as an efficient bifunctional oxygen electrocatalyst. *Catal. Sci. Technol.* **2018**, *8*, 480–485. [CrossRef]
9. Hong, W.; Guo, C.; Koh, S.W.; Ge, J.; Li, H. One-dimensional metal-organic nanowires-derived catalyst of carbon nanobamboos with encapsulated cobalt nanoparticles for oxygen reduction. *J. Catal.* **2020**, *394*, 366–375. [CrossRef]
10. Nguyen, D.C.; Doan, T.L.L.; Prabhakaran, S.; Tran, D.T.; Kim, D.H.; Lee, J.H.; Kim, N.H. Hierarchical Co and Nb dual-doped MoS_2 nanosheets shelled micro-TiO_2 hollow spheres as effective multifunctional electrocatalysts for HER, OER, and ORR. *Nano Energy* **2021**, *82*, 105750. [CrossRef]
11. Gong, W.; Zhang, H.; Yang, L.; Yang, Y.; Wang, J.; Liang, H. Core@shell MOFs derived Co_2P/CoP@NPGC as a highly-active bifunctional electrocatalyst for ORR/OER. *J. Ind. Eng. Chem.* **2021**, *106*, 492–502. [CrossRef]
12. Wang, H.; Qiu, X.; Wang, W.; Jiang, L.; Liu, H. Iron sulfide nanoparticles embedded into a nitrogen and sulfur Co-doped carbon sphere as a highly active oxygen reduction electrocatalyst. *Front. Chem.* **2019**, *7*, 855. [CrossRef] [PubMed]
13. Wang, Q.; Zhang, Z.; Shi, S.; Wu, F.; Zhang, Z.; Li, G.; Suo, Y. Highly active cobalt- and nitrogen-doped carbon derived from ZIF-67@melamine towards oxygen reduction reaction. *J. Electroanal. Chem.* **2021**, *894*, 115397. [CrossRef]
14. Yao, P.; Cao, J.; Gong, X.; Han, C.; Xu, W. ZIF-derived Co–N–S tridoped carbon frameworks for electrocatalytic oxygen reduction reaction. *J. Phys. Chem. C* **2021**, *125*, 9839–9846. [CrossRef]
15. Sun, T.; Tian, B.; Lu, J.; Su, C. Recent advances in Fe (or Co)/N/C electrocatalysts for the oxygen reduction reaction in polymer electrolyte membrane fuel cells. *J. Mater. Chem. A.* **2017**, *5*, 18933–18950. [CrossRef]
16. Hu, H.; Ling, X.; Tan, C.; Lin, J.; Han, X.; Hu, W. Preparation of Ni_3Fe_2@NC/CC integrated electrode and its application in zinc-air battery. *Front. Chem.* **2020**, *8*, 575288. [CrossRef]
17. Guan, Y.; Li, N.; He, J.; Li, Y.; Zhang, L.; Zhang, Q.; Ren, X.; He, C.; Zheng, L.; Sun, X. Tuning and understanding the electronic effect of Co–Mo–O sites in bifunctional electrocatalysts for ultralong-lasting rechargeable zinc–air batteries. *J. Mater. Chem. A* **2021**, *9*, 21716–21722. [CrossRef]
18. Guo, Y.; Huang, Q.; Ding, J.; Zhong, L.; Li, T.-T.; Pan, J.; Hu, Y.; Qian, J.; Huang, S. CoMo carbide/nitride from bimetallic MOF precursors for enhanced OER performance. *Int. J. Hydrogen Energy* **2021**, *46*, 22268–22276. [CrossRef]
19. Guo, J.; Gadipelli, S.; Yang, Y.; Li, Z.; Lu, Y.; Brett, D.; Guo, Z. An efficient carbon-based ORR catalyst from low-temperature etching of ZIF-67 with ultra-small cobalt nanoparticles and high yield. *J. Mater. Chem. A* **2019**, *7*, 3544–3551. [CrossRef]
20. Zhang, J.; Zhang, T.; Ma, J.; Wang, Z.; Liu, J.; Gong, X. ORR and OER of Co–N co-doped carbon-based electrocatalysts enhanced by boundary layer oxygen molecules transfer. *Carbon* **2021**, *172*, 556–568. [CrossRef]
21. Li, G.; Tang, Y.; Fu, T.; Xiang, Y.; Xiong, Z.; Si, Y.; Guo, C.; Jiang, Z. S, N co-doped carbon nanotubes coupled with CoFe nanoparticles as an efficient bifunctional ORR/OER electrocatalyst for rechargeable Zn-air batteries. *Chem. Eng. J.* **2022**, *429*, 132174. [CrossRef]
22. Awadallah-F, A.; Al-Muhtaseb, S. Carbon Nanoparticles-Decorated Carbon Nanotubes. *Sci. Rep.* **2020**, *10*, 4878. [CrossRef] [PubMed]
23. Ye, H.; Li, L.; Liu, D.; Fu, Q.; Zhang, F.; Dai, P.; Gu, X.; Zhao, X. Sustained-release method for the directed synthesis of ZIF-derived ultrafine Co-NC ORR catalysts with embedded Co quantum dots. *ACS Appl. Mater. Inter.* **2020**, *12*, 57847–57858. [CrossRef] [PubMed]
24. Mou, Q.; Xu, Z.; Wang, G.; Li, E.; Liu, J.; Zhao, P.; Liu, X.; Li, H.; Cheng, G. A bimetal hierarchical layer structure MOF grown on Ni foam as a bifunctional catalyst for the OER and HER. *Inorg. Chem. Front.* **2021**, *8*, 2889–2899. [CrossRef]
25. Liu, Z.; Andrade, A.M.; Grewal, S.; Nelson, A.J.; Thongrivong, K.; Kang, H.-S.; Li, H.; Nasef, Z.; Diaz, G.; Lee, M.H. Trace amount of ceria incorporation by atomic layer deposition in Co/CoO_x-embedded N-doped carbon for efficient bifunctional oxygen electrocatalysis: Demonstration and quasi-operando observations. *Int. J. Hydrog. Energy* **2021**, *46*, 38258–38269. [CrossRef]

26. Duan, Y.; Wang, L.; Zhang, J.; Sun, C.; Wen, R.; Dou, M. Surface Engineering Route to Non-pyrolysis MOFs with High-Density Co–N_x Sites and 3D Conductive Networks for Efficient Oxygen Reduction. *ACS Appl. Energy Mater.* **2023**, *6*, 3244–3250. [CrossRef]
27. Li, L.; Han, G.; Wen, Y.; Liu, Y.; Xiao, R.; Zhang, W.; Kong, F.; Du, L.; Ma, Y.; Zuo, P.; et al. Solvent effect to modulate nitrogen dopant in Co-N-C catalysts for oxygen reduction reaction acceleration. *Fuel* **2023**, *345*, 128199. [CrossRef]
28. Liang, L.; Jin, H.; Zhou, H.; Liu, B.; Hu, C.; Chen, D.; Wang, Z.; Hu, Z.; Zhao, Y.; Li, H.; et al. Cobalt single atom site isolated Pt nanoparticles for efficient ORR and HER in acid media. *Nano Energy* **2021**, *88*, 106221. [CrossRef]
29. Jia, R.; Xia, M.; Tang, L.; Yu, L.; Yang, Y.; Zhang, Y.; Bo, X.; Zhou, S.; Tu, Y.; Deng, D. Single-Atomic Ir and Mo Co-Confined in a Co Layered Hydroxide Nanobox Mutually Boost Oxygen Evolution. *ACS Catal.* **2022**, *12*, 13513–13522. [CrossRef]
30. Sathiyan, K.; Mondal, T.; Mukherjee, P.; Patra, S.; Pitussi, I.; Kornweitz, H.; Bar-Ziv, R.; Zidki, T. Enhancing the catalytic OER performance of MoS_2 via Fe and Co doping. *Nanoscale* **2022**, *14*, 16148–16155. [CrossRef]
31. Liu, J.; Zhang, H.; Meng, J.; Han, C.; Liu, F.; Liu, X.; Wu, P.; Liu, Z.; Wang, X.; Mai, L. A "MOFs plus ZIFs" strategy toward ultrafine Co nanodots confined into superficial N-doped carbon nanowires for efficient oxygen reduction. *ACS Appl. Mater. Interfaces* **2020**, *12*, 54545–54552. [CrossRef] [PubMed]
32. Feng, C.; Xie, Y.; Qiao, S.; Guo, Y.; Li, S.; Zhang, L.; Wang, W.; Wang, J. Porous MoWN/MoWC@NC Nano-octahedrons synthesized via confined carburization and vapor deposition in MOFs as efficient trifunctional electrocatalysts for oxygen reversible catalysis and hydrogen production in the same electrolyte. *J. Colloid Interface Sci.* **2021**, *601*, 626–639. [CrossRef] [PubMed]
33. Xiao, Y.; Deng, S.; Li, M.; Zhou, Q.; Xu, L.; Zhang, H.; Sun, D.; Tang, Y. Immobilization of Fe-doped Ni_2P particles within biomass agarose-derived porous N, P-carbon nanosheets for efficient bifunctional oxygen electrocatalysis. *Front. Chem.* **2019**, *7*, 523. [CrossRef] [PubMed]
34. Shi, Q.; Liu, Q.; Ma, Y.; Fang, Z.; Liang, Z.; Shao, G.; Tang, B.; Yang, W.; Qin, L.; Fang, X. High-performance trifunctional electrocatalysts based on FeCo/Co_2P hybrid nanoparticles for zinc–air battery and self-powered overall water splitting. *Adv. Energy Mater.* **2020**, *10*, 1903854. [CrossRef]
35. Liu, H.; Yang, D.H.; Wang, X.Y.; Zhang, J.; Han, B.H. N-doped graphitic carbon shell-encapsulated FeCo alloy derived from metal-polyphenol network and melamine sponge for oxygen reduction, oxygen evolution, and hydrogen evolution reactions in alkaline media. *J. Colloid Interface Sci.* **2021**, *581*, 362–373. [CrossRef] [PubMed]
36. Ju, Q.; Ma, R.; Pei, Y.; Guo, B.; Liu, Q.; Zhang, T.; Yang, M.; Wang, J. Nitrogen-doped carbon spheres decorated with CoS_x nanoparticles as multifunctional electrocatalysts for rechargeable zn-air battery and overall water splitting. *Mater. Res. Bull.* **2020**, *125*, 110770. [CrossRef]
37. Rai, V.; Lee, K.P.; Safanama, D.; Adams, S.; Blackwood, D.J. Oxygen reduction and evolution reaction (ORR and OER) bifunctional electrocatalyst operating in a wide pH range for cathodic application in Li–air Batteries. *ACS Appl. Energy Mater.* **2020**, *3*, 9417–9427. [CrossRef]
38. Zhou, Y.; Zhang, Y.; Xu, X.; Zhao, S.; Guo, Z.; Wu, K.H.; Tan, C. Wang. Bimetallic metal-organic framework derived metal-carbon hybrid for efficient reversible oxygen electrocatalysis. *Front. Chem.* **2019**, *7*, 747. [CrossRef]